Maoyi Zhang
State Key Laboratory of Nonlinear Mechanics,
Institute of Mechanics,
Chinese Academy of Sciences,
Beijing 100190, China;
School of Engineering Science,
University of Chinese Academy of Sciences,
Beijing 100049, China

Hao Liu
State Key Laboratory of Nonlinear Mechanics,
Institute of Mechanics,
Chinese Academy of Sciences,
Beijing 100190, China;
Institute of Solid Mechanics,
Beihang University (BUAA),
Beijing 100191, China

Peng Cao
Department of Hydraulic Engineering,
Tsinghua University,
Beijing 100084, China

Bin Chen
Institute of Solid Mechanics,
Beihang University (BUAA),
Beijing 100191, China

Jianqiao Hu
State Key Laboratory of Nonlinear Mechanics,
Institute of Mechanics,
Chinese Academy of Sciences,
Beijing 100190, China

Yuli Chen
Institute of Solid Mechanics,
Beihang University (BUAA),
Beijing 100191, China

Bing Pan
Institute of Solid Mechanics,
Beihang University (BUAA),
Beijing 100191, China

Jonathan A. Fan
Department of Electrical Engineering,
Stanford University,
Stanford, CA 94305

Rui Li[1]
State Key Laboratory of Structural Analysis for
Industrial Equipment,
Department of Engineering Mechanics,
International Research Center for
Computational Mechanics,
Dalian University of Technology,
Dalian 116024, China
e-mail: ruili@dlut.edu.cn

Lijuan Zhang[1]
State Key Laboratory of Nonlinear Mechanics,
Institute of Mechanics,
Chinese Academy of Sciences,
Beijing 100190, China
e-mail: zhanglijuan@imech.ac.cn

Yewang Su[1]
State Key Laboratory of Nonlinear Mechanics,
Institute of Mechanics,
Chinese Academy of Sciences,
Beijing 100190, China;
School of Engineering Science,
University of Chinese Academy of Sciences,
Beijing 100049, China;
State Key Laboratory of Structural Analysis for
Industrial Equipment,
Department of Engineering Mechanics,
International Research Center for
Computational Mechanics,
Dalian University of Technology,
Dalian 116024, China;
State Key Laboratory of Digital Manufacturing
Equipment and Technology,
Huazhong University of
Science and Technology,
Wuhan 430074, China
e-mail: yewangsu@imech.ac.cn

Strain-Limiting Substrates Based on Nonbuckling, Prestrain-Free Mechanics for Robust Stretchable Electronics

Stretchable electronics based on inorganic materials are an innovative technology with potential applications for many emerging electronic devices, due to their combination of stretchable mechanics and high electronic performance. The compliant elastomeric substrate, on which the brittle electronic components are mounted, plays a key role in achieving stretchability. However, conventional elastomeric substrates can undergo excessive mechanical deformation, which can lead to active component failure. Here, we introduce a simple and novel strategy to produce failure-resistant stretchable electronic platforms by bonding a thin film of stiff material, patterned into a serpentine network layout, to the elastomeric substrate. No prestraining of the substrate is required, and these systems offer sharp bilinear mechanical behavior and high ratio of tangent-to-elastic moduli. We perform comprehensive theoretical, numerical, and experimental studies on the nonbuckling-based prestrain-free design, and we analyze the key parameters impacting the mechanical behavior of a strain-limiting substrate. As a device-level demonstration, we experimentally fabricate and characterize skin-mountable stretchable copper (Cu) electrodes for electrophysiological monitoring. This study paves the way to high performance stretchable electronics with failure-resistant designs.
[DOI: 10.1115/1.4038173]

Keywords: strain-limiting substrates, nonbuckling, prestrain-free design, stretchable electronics

1 Introduction

Stretchable electronics are an emergent device platform that have applications in many technologies, such as stretchable and foldable silicon-integrated circuits [1,2], electronic eye cameras [3,4], epidermal electronics [5], fingertip electronics [6,7], transient electronics [8,9], stretchable batteries [10], conformal piezo-electric energy harvesters [11,12], soft robots [13,14], and prostheses [15,16]. For stretchable electronics based on high performance inorganic materials, the key strategy for achieving stretchability is integrating the brittle, thin-film electronic components onto a compliant elastomeric substrate, which can accommodate large deformations.

A central challenge with stretchable electronic devices is preventing active device failure due to overstretching the substrate. The fracture strain of inorganic active components is on the order of only 1%, and these fracture strains can typically be reached when the substrate is modestly strained, to levels far below its ultimate fracture strain. Strain-limiting substrates offer one possible solution to the challenge. These substrates display compliant responses to stretching when deformed below a certain threshold strain, but stiffen when the applied strain is above the threshold, thereby preventing excessive substrate deformation and protecting the active components against fracture. A strain-limiting substrate should ideally exhibit a bilinear stress–strain behavior that supports a low elastic stiffness (i.e., compliant response) at relatively small applied strains and a high tangent stiffness (i.e., stiffening response) at large strain.

Conventional strain-limiting structural designs are based on curved microstructures in network layouts [17,18], helical designs with natural or synthetic constructions [19,20], and textile designs manufactured by knitting, weaving or braiding [21,22]. Jang et al. [18] proposed the design idea of binding serpentine networks on soft substrates to tune the stress–strain curves of the composites, while this study aims to tune geometry to achieve the stronger strain-limiting effect. While effective for some applications, most of these design schemes only provide a smooth "J-shaped" stress–strain behavior, and they support relatively small ratios (~10) of tangent-to-elastic moduli. These limitations were recently addressed in a scheme proposed by Ma et al. [23], who implemented a strain-limiting substrate by transferring a thin film or mesh of high stiffness material onto a prestrained compliant substrate. Upon release of the prestrain, the high stiffness structure became wrinkled. At small strain levels, the system displayed low elastic stiffness similar to that of the compliant substrate, due to the negligible stiffness of the wrinkled film. Beyond an applied strain in which the film became flat, the system supported high tangent stiffness. This strain-limiting substrate supports sharp bilinear behavior, represented by a clear transition point in the stress–strain curve, and a very high ratio ($>10^3$) of tangent-to-elastic moduli, which is ideal for many applications. It is of tremendous interest to identify strain-limiting substrates that possess such specifications without the requirement for prestraining, which can significantly complicate the fabrication process.

In this paper, we introduce a novel nonbuckling-based prestrain-free design for strain-limiting substrates that exhibit sharp bilinear mechanical behavior and a high ratio of tangent-to-elastic moduli. In our approach, we bond a thin film of stiff material, patterned into a serpentine network layout, to a prestrain-free compliant substrate without any mechanical pretreatment. The design of the film layout is critical in this strategy. Compared to schemes based on substrate prestraining, ours offers a much simpler pathway to fabrication.

In the following, we present comprehensive theoretical, numerical, and experimental studies on our prestrain-free design. We investigate the main factors affecting the mechanical behavior of a strain-limiting substrate, namely thickness and material of the compliant substrate, loading conditions of the system, and central angle, thickness, width, and cross-sectional dimensions of the curved network layout. Based on the in-depth knowledge gained

from our theoretical and numerical modeling, we identify an effective strain-limiting substrate design and demonstrate its use in skin-mountable stretchable copper (Cu) electrodes for precision measurement of electrophysiological signals.

2 Results and Discussion

A schematic illustration of our nonbuckling-based prestrain-free design for strain-limiting stretchable electronics is shown in Fig. 1(a). Here, a thin film of mechanically stiff material (e.g., polyimide (PI)) is patterned into a serpentine network layout and bonded to a compliant elastomeric substrate (e.g., silbone) without prestrain. The key design parameters of this film-substrate system include the substrate thickness t_{sub}, film thickness t_{PI}, period of the network mesh T, width of the wires w_{PI}, central angle of the half-periodic wires α, and arc radius R.

Figures 1(b)–1(g) show the experimental preparation of a representative strain-limiting substrate (see Appendix A for experimental details). First, a layer of polyvinylpyrrolidone (PVP) is coated onto a piece of paper (Fig. 1(b)), followed by casting a 500 μm thick silbone layer (Fig. 1(c)). The system is then immersed in water to dissolve the PVP layer, to separate the silbone layer from the paper (Fig. 1(d)). A patterned PI mesh with dimensions $15T \times 15T$, $w_{PI} = 50\,\mu m$, $t_{PI} = 100\,\mu m$, and $\alpha = 180$ deg, is fabricated via laser cutting and placed on the top of the silbone (Fig. 1(e)) to form the PI/silbone substrate. The PI structure adheres to the silbone by van der Waals forces. The strain-limiting substrate (Fig. 1(f)) is mechanically tested in a microtensile material-testing machine and is uniaxially stretched to yield a stress–strain curve (Fig. 1(g)).

Figure 1(h) shows the measured stress–strain curve and the theoretical curve obtained from finite element analysis (FEA, see details in Appendix B for analytic and numerical modeling) for our representative strain-limiting substrate. Favorable agreement is observed. These curves indicate that the substrate displays a bilinear stress–strain behavior, which offers a low elastic stiffness (compliant response) at small applied strain and a high tangent stiffness (stiffening response) at large strain. The aforementioned behavior is attributed to the satisfaction of two requirements: (i) before the traces in the PI serpentine network are stretched to the point of straightening (i.e., the transition point), its stiffness is lower than or comparable to the stiffness of the silbone substrate; and (ii) beyond the transition point, the stiffness of the PI serpentine network is much higher than the silbone substrate. Different mechanical behaviors are displayed in the two stages. Before the transition point in the stress–strain curve, mechanical deformation in the PI network can be described as in-plane bending, with the bending stiffness proportional to $t_{PI}w_{PI}^3$. After the transition point, the PI traces straighten and are stretched with a tensile stiffness proportional to $t_{PI}w_{PI}$. Strong bilinear stress–strain behavior is achieved when the traces in the PI network possess a relatively small w_{PI} and large t_{PI}.

Quantitative study is indispensable to understanding the complex mechanical behavior of a strain-limiting substrate, as well as its optimal design. To begin, we focus on a simple configuration consisting of a single PI wire containing continuous arcs, mounted on the silbone substrate. Uniaxial tension is applied, as shown in Fig. 2(a), and a unit cell of the PI wire (inset of Fig. 2(a)) is analyzed to investigate the strain-limiting effect. For the $2000 \times 2000 \times 500\,\mu m^3$ silbone substrate, the Young's modulus and cross-sectional area are $E_{sub} = 3$ kPa and $2000 \times 500\,\mu m^2$, respectively. Following the guidelines outlined in the previous paragraph, the PI trace is specified to be relatively narrow (width $w_{PI} = 25\,\mu m$) and thick (thickness $t_{PI} = 100\,\mu m$), with an arc radius $t_{PI} = 100\,\mu m$, Young's modulus $E_{PI} = 2500$ MPa, and cross-sectional area of $2500\,\mu m^2$.

Our FEA modeling is conducted to capture the system mechanics as the PI trace stretches from the initial stress-free state to straight state (Fig. 2(b)). Initially, the system displays a compliant response, and it then stiffens after it crosses the transition point.
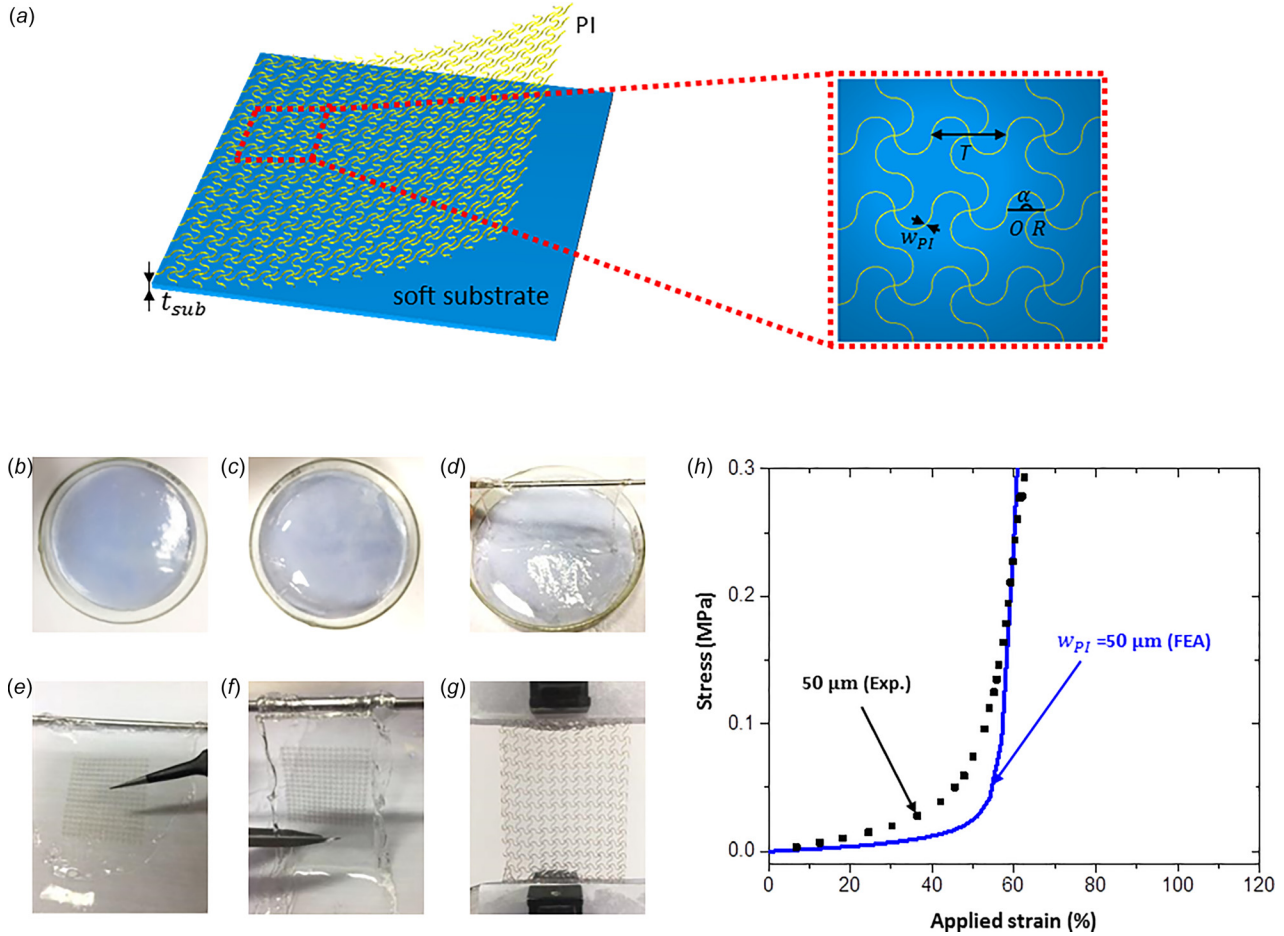
Fig. 1 Schematic illustration of novel nonbuckling-based prestrain-free design for strain-limiting substrate of stretchable electronics. (*a*) Demonstration of the strain-limiting structure. (*b*)–(*g*) Fabrication of a representative strain-limiting substrate. (*h*) Measured stress-strain relationship in comparison with that from FEA.

Interestingly, there is no buckling induced in the PI trace due to its narrow and thick aspect ratio (buckling is unlikely to happen when the thickness/width ratio is large enough (e.g., $>\sim 1$), as pointed out in Ref. [24]). To understand this behavior, we investigate a simplified analytic model that captures the key mechanics (Figs. 2(*c*) and 2(*d*)). Without coupling between the PI trace and silbione, the straightening of the PI structure corresponds to the transition strain, defined by

$$\varepsilon_t = \frac{\alpha - 2\sin\frac{\alpha}{2}}{2\sin\frac{\alpha}{2}} \tag{1}$$

For the cell with continuous semicircles, $\varepsilon_t = 57\%$, which agrees very well with the value calculated from FEA ($\sim 57\%$ transition strain) in Fig. 2(*b*). We further analyze a quarter arc section of the PI (Fig. 2(*c*)) and calculate the stress–strain relationship of the PI/silbione system to be

$$\sigma = \begin{cases} \left[E_{\text{sub}} + \dfrac{E_{\text{PI}} t_{\text{PI}} w_{\text{PI}}^3 \sin\frac{\alpha}{2}}{3 t_{\text{sub}} T R^2 (\alpha + \sin\alpha)} \right] \varepsilon & \text{for} \quad \varepsilon \leq \varepsilon_t \\[3em] \left[E_{\text{sub}} + \dfrac{E_{\text{PI}} t_{\text{PI}} w_{\text{PI}}^3 \sin\frac{\alpha}{2}}{3 t_{\text{sub}} T R^2 (\alpha + \sin\alpha)} \right] \varepsilon_t + \left(E_{\text{sub}} + E_{\text{PI}} \dfrac{t_{\text{PI}} w_{\text{PI}}}{t_{\text{sub}} T} \right) (\varepsilon - \varepsilon_t) & \text{for} \quad \varepsilon \geq \varepsilon_t \end{cases} \tag{2}$$

Here, $\sigma = 0.00466\varepsilon$ MPa for $\varepsilon \leq 57\%$ (before the transition point) and $\sigma = 6.25\,\varepsilon - 3.56$ MPa for $\varepsilon \geq 57\%$ (after the transition point). Further details involving the calculation are in Appendix B.

We can further quantify our design criteria for strain-limiting substrates by examining Eq. (2) in the context of the requirements (i) and (ii) defined earlier. From (i), $(E_{PI}t_{PI}w_{PI}^3 \sin(\alpha/2)/(3t_{sub}TR^2(\alpha + \sin\alpha)) \leq E_{sub}$ should be satisfied, which yields

$$\frac{\sin\frac{\alpha}{2}}{3(\alpha + \sin\alpha)} \times \frac{E_{PI}t_{PI}w_{PI}^3}{E_{sub}t_{sub}TR^2} \leq 1 \qquad (3)$$
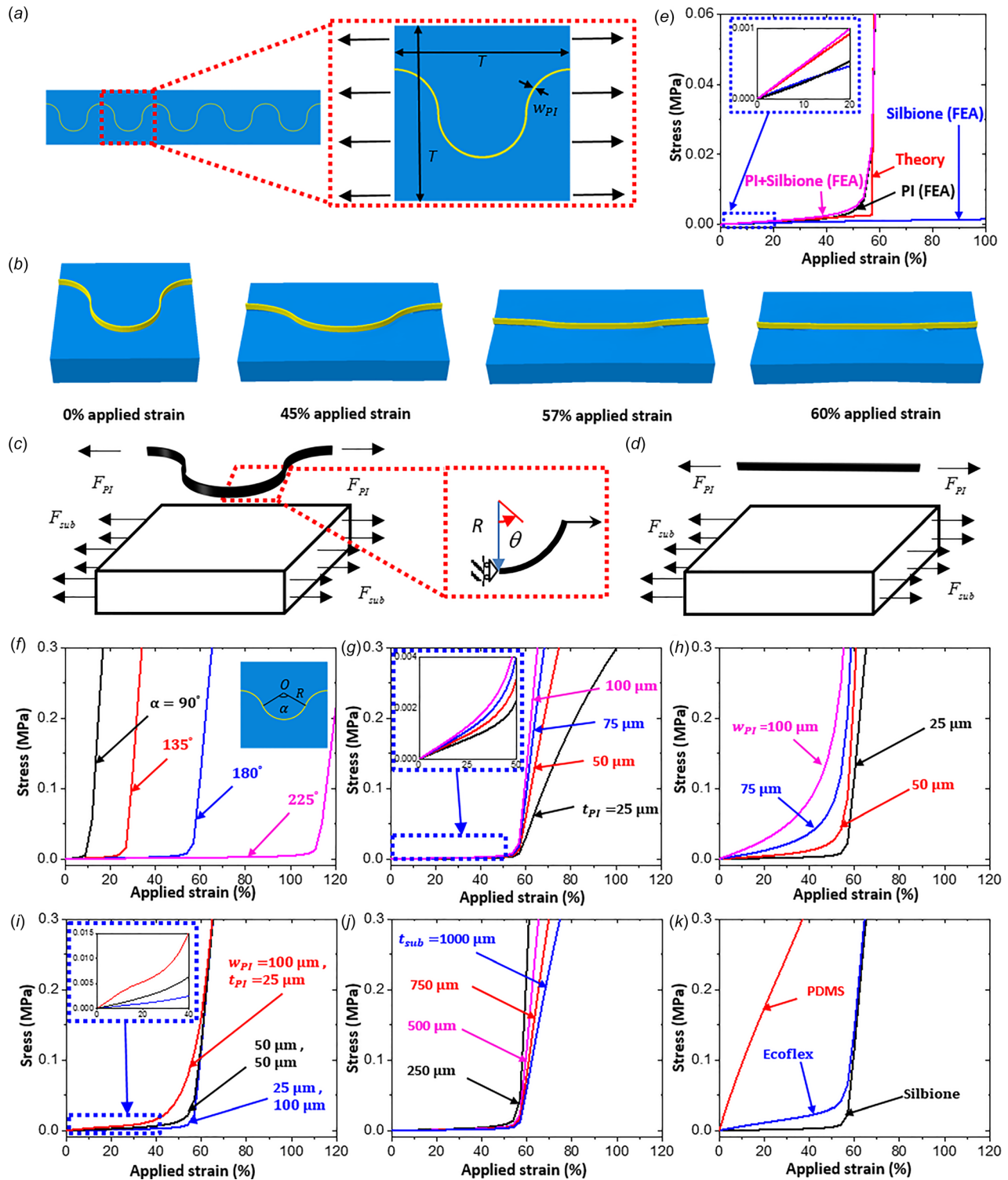

Fig. 2 Quantitative study of a strain-limiting substrate utilizing a single PI trace. (*a*) Configuration of a single PI trace mounted on a silbione substrate. (*b*) FEA images of a single unit cell of the system under different strain levels. (*c*) and (*d*) An analytic mechanics model for the unit cell. (*e*) Stress–strain curves of the PI/silbione system from analytic modeling and FEA. (*f*)–(*k*) Effects on the stress–strain relationship of the (*f*) central angle, (*g*) PI thickness, (*h*) PI width, (*i*) cross-sectional dimensions, (*j*) substrate thickness, and (*k*) material of the substrate.

From (ii), $E_{\text{sub}} + E_{\text{PI}}t_{\text{PI}}w_{\text{PI}}/t_{\text{sub}}T \gg E_{\text{sub}}$ should be satisfied, which yields

$$\frac{E_{\text{PI}}t_{\text{PI}}w_{\text{PI}}}{E_{\text{sub}}t_{\text{sub}}T} \gg 1 \qquad (4)$$

For the design in Fig. 2(b), Eqs. (3) and (4) give $0.553 < 1$ and $2083 \gg 1$, respectively, indicating that our design criteria for effective strain-limiting substrates are satisfied.

Analytic stress–strain curves of the PI/silbone system based on Eq. (2) are displayed in Fig. 2(e), together with plots from FEA with only the PI trace, only silbone, and the coupled PI/silbone system. It is seen that the stress–strain curve of the PI trace (black line) is lower than or comparable to that of silbone (blue line) at strain levels below the transition point, but is much higher than that of silbone above the transition point. Similar trends are observed for the stress–strain curve of the PI/silbone system (purple line), as compared to that of silbone (blue line). In general, the analytic model agrees very well with FEA, and both curves display similar transition points. We note minor discrepancies near the transition point, arising due to the decoupling between the substrate and PI trace in our analytic model.

Figures 2(f)–2(k) illustrate the impact of the central angle α, PI thickness t_{PI}, PI width w_{PI}, cross-sectional dimensions t_{PI} and w_{PI}, substrate thickness t_{sub}, and substrate material on the stress–strain relationship of the PI-substrate system by FEA modeling. Figure 2(f) shows that transition angle strongly scales with central angle. For

example, PI traces with $\alpha = 225$ deg possess a transition strain near $\sim 110\%$, while PI traces with $\alpha = 90$ deg possess a transition strain of only $\sim 10\%$. Figure 2(g) shows that variations in PI thickness produce small changes in the transition strains in the stress–strain curves. Thicker PI will generally lead to sharper transitions, which is desirable for strain-limiting, but also raises the overall stress level both before and after the transition point (inset of Fig. 2(g)).

Figure 2(h) indicates that as the width of the PI trace increases, the transition point becomes less abrupt as a function of strain. As such, relatively narrow PI trace widths are required for the system to support sharp, bilinear stress–strain behavior. This observation is also observed in Fig. 2(i), in which the cross-sectional area of the PI trace is fixed to 2500 μm^2. The narrower and thicker PI traces display sharp stress–strain curves and relatively low stress levels below the transition point (inset of Fig. 2(i)). Figure 2(j) shows that a smaller substrate thickness yields a sharper response, since the tangent stiffness at strains larger than the transition point increases with reduced t_{sub}. In Fig. 2(k), two common elastomeric substrates (ecoflex, with $E_{\text{ecoflex}} = 60$ kPa; and polydimethylsiloxane (PDMS), with $E_{\text{PDMS}} = 1$ MPa) with the same size ($2000 \times 2000 \times 500 \, \mu m^3$) are examined and compared with silbone. These stress–strain curves show that silbone systems support a larger transition strain and lower stress level compared to ecoflex. PDMS is undesirable because there is no transition point, due to its high elastic stiffness.

Figure 3 demonstrates three different loading conditions (uniaxial, 45 deg, and biaxial tensions) for a strain-limiting PI/silbone
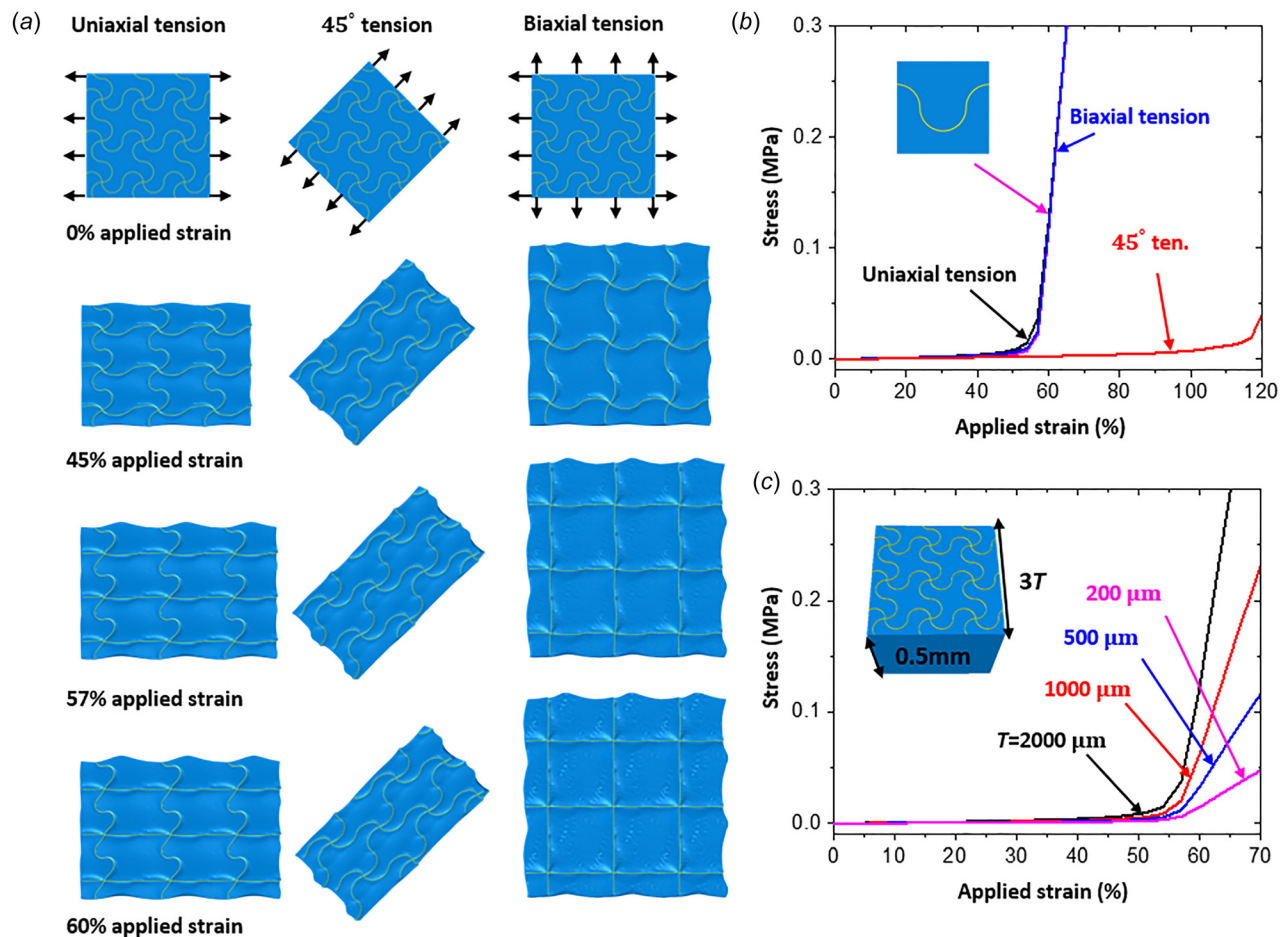

Fig. 3 Representative loading conditions (uniaxial, 45 deg, and biaxial tensions) for a strain-limiting PI/silbone substrate. (a) FEA results of the strain-limiting substrate under four applied strains (0%, 45%, 57%, and 60%). (b) Stress–strain curves of the strain-limiting substrate under different loading conditions, with comparisons to the unit cell model proposed in Fig. 2. (c) Size effect on the stress–strain curves of the strain-limiting substrates, where $R = 500$, 250, 125, and 50 μm, $w_{\text{PI}} = 25$, 12.5, 6.25, and 2.5 μm, and $t_{\text{PI}} = 100$, 50, 25, and 10 μm for $T = 2000$, 1000, 500, and 200 μm, respectively.
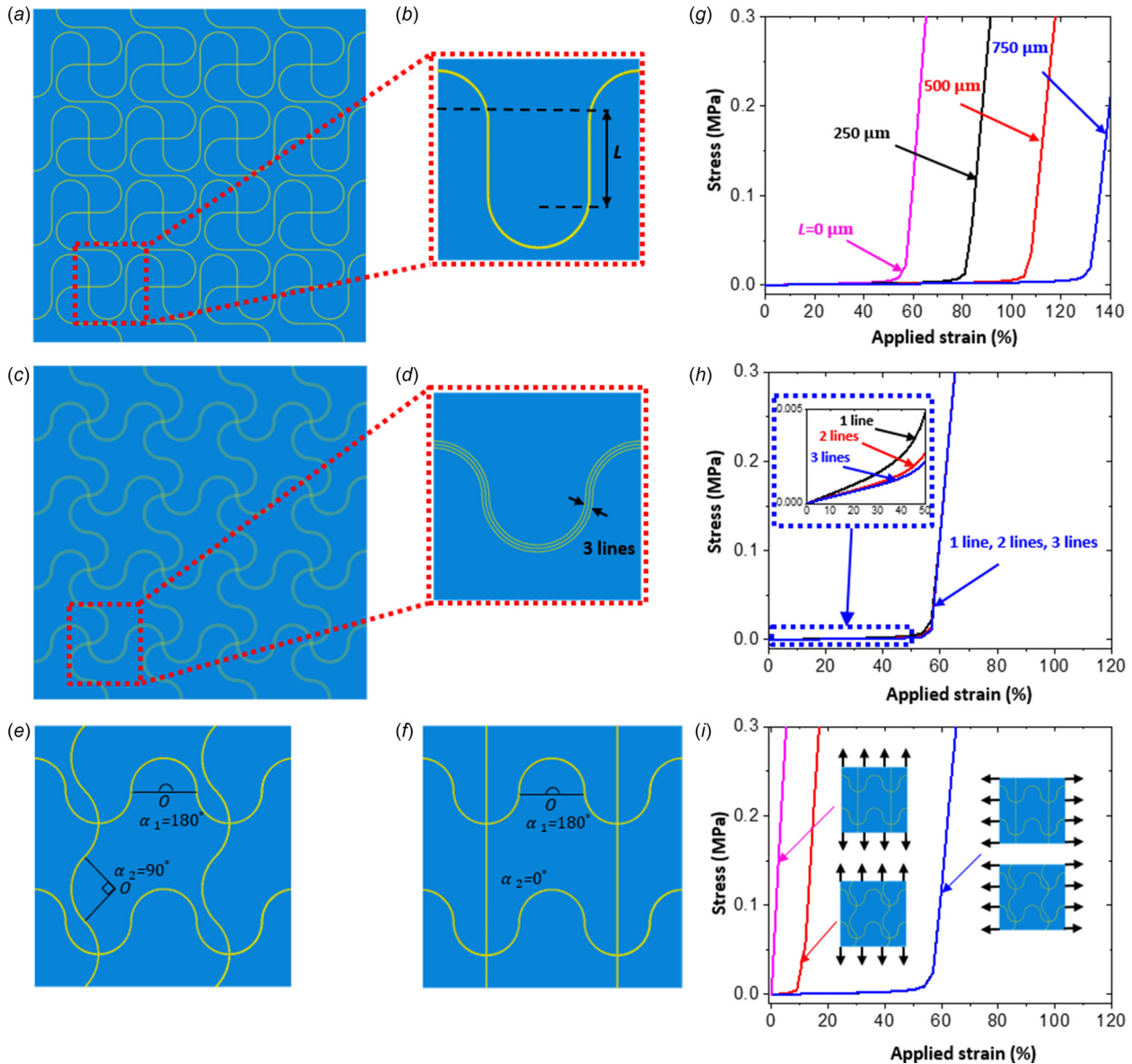
Fig. 4 Alternative geometric designs of strain-limiting substrates. (*a*) and (*b*) Designs with differing PI trace lengths within a unit cell. (*c*) and (*d*) Designs based on splitting a PI trace into multiple adjacent traces. (*e*) and (*f*) Designs based on differing central angles in the PI arc sections. (*g*) Impact of PI length on the stress–strain relationship. (*h*) Impact of number of adjacent PI traces on the stress–strain relationship. (*i*) Stress–strain curves of the strain-limiting substrates shown in (*e*) and (*f*), under different loading conditions.

substrate containing PI traces arranged in a square lattice. The dimensions of a unit cell are the same as those in Fig. 2(*a*). The FEA results of a substrate stretched in different configurations for four representative applied strains (0, 45%, 57%, and 60%) are displayed in Fig. 3(*a*). Periodic boundary conditions are applied to reduce the computational cost, without loss of computational accuracy. These simulations indicate that the transition strain for uniaxial stretching in the 45 deg direction is much larger than those under other loading conditions (Fig. 3(*b*)), revealing an anisotropic mechanical behavior in the system. The stress–strain curves for these mesh samples stretched uniaxially and biaxially agree well with the curve for a linear PI trace presented in Fig. 2(*a*), indicating that the unit cell model proposed in Fig. 2 can apply to understanding square mesh layouts. The size effect is also examined by equal scaling of the PI mesh, with the stress–strain relationships plotted for the system with different PI scales (Fig. 3(*c*)), which shows that scaling up the PI (i.e., linearly increasing the period T, thickness t_{PI}, and width w_{PI}) can stiffen

the system and sharpen the bilinear behavior. This indicates that PI mesh scaling can be used to optimize our strain-limiting systems.

We further study other geometric variations of the PI mesh network, with results summarized in Fig. 4. The following PI wire characteristics are examined: length (Figs. 4(*a*) and 4(*b*)), number of PI traces within an arc section (Figs. 4(*c*) and 4(*d*)), and central angle (Figs. 4(*e*) and 4(*f*)). We see in Fig. 4(*g*) that increasing the length of the PI trace within each unit cell increases the value of the transition strain, without impacting the stress level. For example, $L = 750\,\mu m$ corresponds to a transition strain as large as ~130%, compared to ~50% transition strain for $L = 0$. In Fig. 4(*h*), we find that when we split a PI trace into multiple separated traces, the strain level before the transition point lowers, without impacting the high stiffness level at strains above the transition point. In Fig. 4(*i*), the designs of the PI traces with two different central angles (Fig. 4(*e*) and 4(*f*)) are examined, and the substrates are uniaxially stretched in the horizontal and vertical
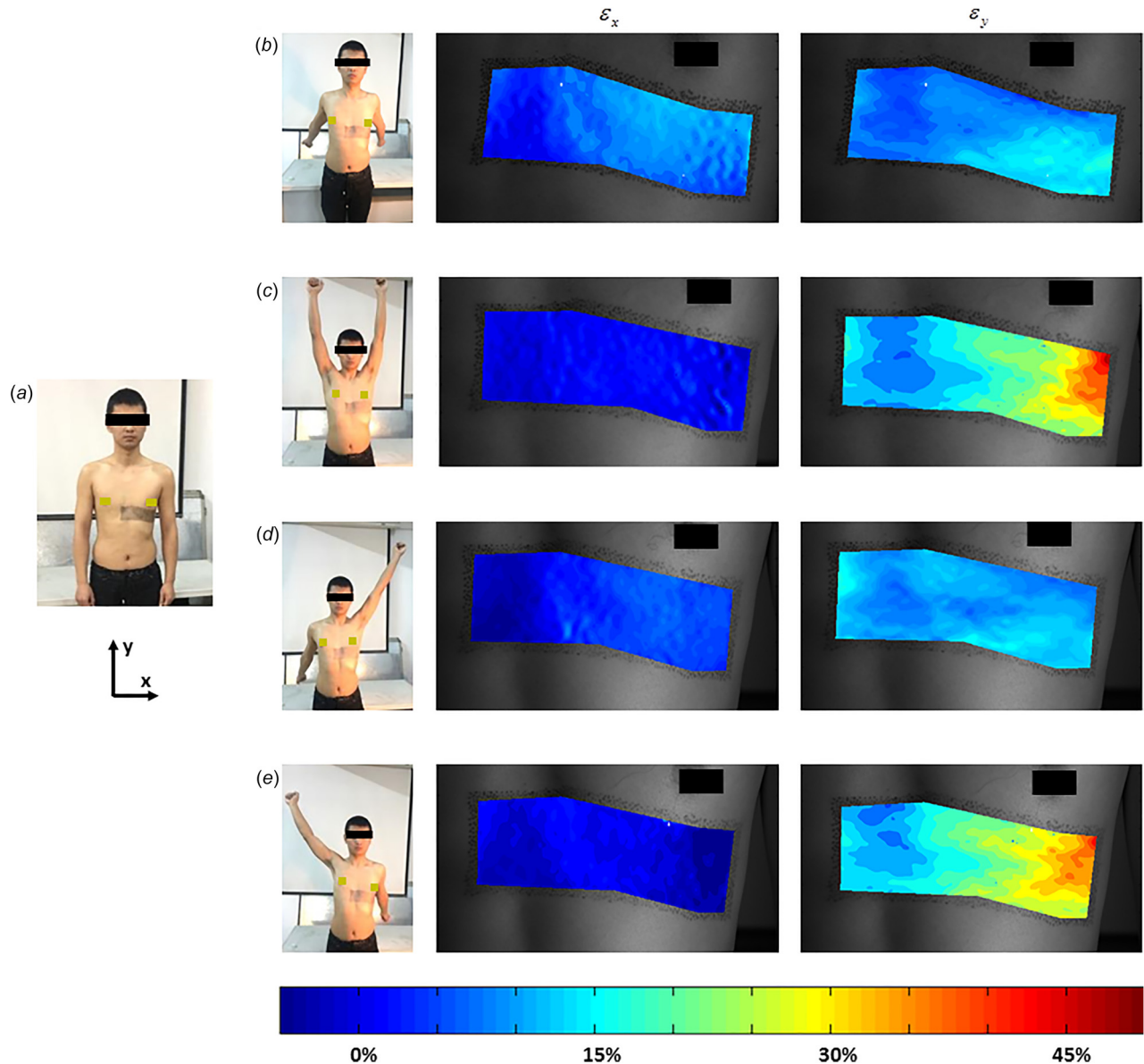
Fig. 5 Strain distribution measurements on the chest based on digital image correlation method. (*a*) Image of fully relaxed body. (*b*)–(*e*) Strain distributions measured during four extreme body movements (described in detail in the main text).

directions. We find that the transition strain in the horizontal direction is much larger than that in the vertical direction for both designs, and it depends mainly on the PI mesh configuration in the loading direction. Along the horizontal direction, both samples have identical horizontal-oriented PI trace layouts and exhibit the same stress–strain behavior (overlapped blue lines in Fig. 4(*i*)).

To demonstrate a device-level application of our strain-limiting substrate, we integrate a skin-mountable stretchable Cu electrode with our substrate and monitor electrophysiological signals from the heart (electrocardiogram) and muscle tissue (electromyogram (EMG)) (see Appendix A for experimental details). Our first task is to measure the strain distribution on the left chest of an adult human subject, which we achieve using the digital image correlation method, to gauge the mechanical environment of our electrodes (Fig. 5). Deformation of the human chest is represented by four extreme body movements from the initial strain-free state, when the body is fully relaxed (Fig. 5(*a*), coordinate system shown at the bottom).

In Fig. 5(*b*), the subject brings his drooping arms backward (left image), and the strain contours are illustrated during the movement (middle and right images). The maximum strain in the

contour plot measured in the *x*-direction is $\varepsilon_x = 15.9\%$ and is $\varepsilon_y = 19.2\%$ along the *y*-direction. In Fig. 5(*c*), the subject lifts his arms backward (left image), and the strain distributions (middle and right images) display maximum strains of $\varepsilon_x = 6.9\%$ and $\varepsilon_y = 49.5\%$ along the *x*- and *y*-directions, respectively. In the other two movements, the subject lifts his left arm and droops his right arm backward (Fig. 5(*d*)), then switches the positions of the two arms (Fig. 5(*e*)). The corresponding strain distributions display maximum strains of $\varepsilon_x = 9.6\%$ and $\varepsilon_y = 17.5\%$ in the first case and $\varepsilon_x = 15.3\%$ and $\varepsilon_y = 44.7\%$ in the second case along the *x*- and *y*-directions, respectively. This analysis indicates that for certain extreme motions, the local strain levels at parts of the chest can be very high (40%+) and can be damaging to skin-mounted electronics without a strain-limiting substrate.

We fabricate our stretchable Cu electrode system (Fig. 6(*a*)) by mounting two laser-cut Cu electrode networks (layout shown on the top right) on top of the silbione substrate, and one laser-cut network PI on the bottom of the substrate (layout shown on the bottom right). Our Cu mesh network has $L = 1350\,\mu\text{m}$, $R = 900\,\mu\text{m}$, $w_{\text{Cu}} = 50\,\mu\text{m}$, $t_{\text{Cu}} = 30\,\mu\text{m}$, and $\alpha = 180\,\text{deg}$. Under uniaxial tension, FEA modeling (Figs. 6(*b*)–6(*d*)) indicates that
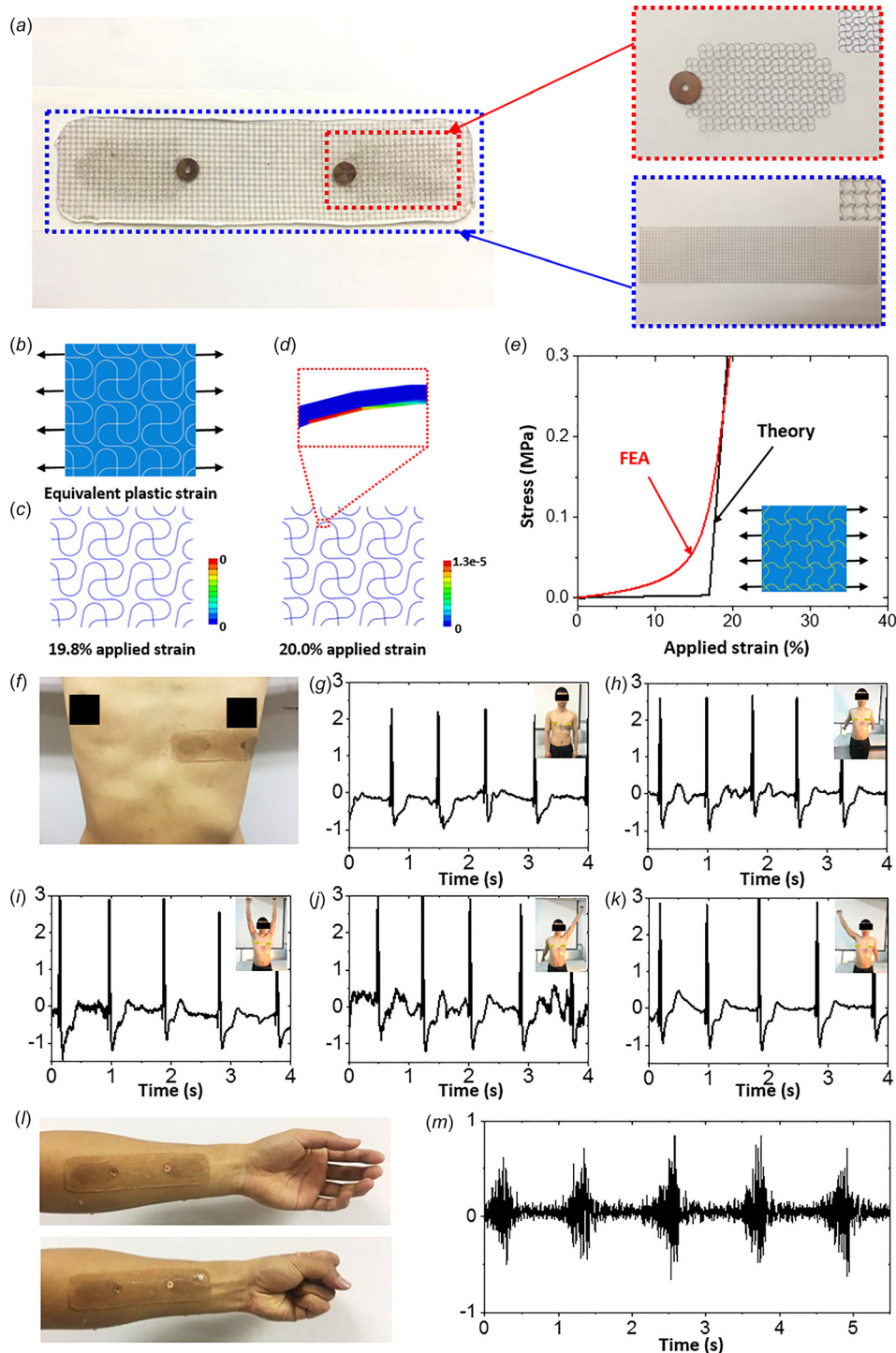
Fig. 6 Strain-limiting substrate-based stretchable Cu electrode for electrophysiological signals measurement. (*a*) Optical image of the electrode. (*b*) Cu electrode network under uniaxial tension. (*c*)–(*d*) FEA results of Cu wires when stretched to 19.8% and 20% applied strain. (*e*) Stress–strain curve of the PI/silbione system. (*f*) Image of the electrode adhered to a chest. (*g*)–(*k*) Electrocardiograms of the subject when fully relaxed and during extreme body movements. (*l*) Image of the electrode adhered inside the forearm. (*m*) Electromyogram during hand clenches.

the Cu wires undergo plastic yield when stretched to 20% applied strain (Fig. 6(*d*)), while no plastic deformation is detected right below that strain, e.g., at 19.8% (Fig. 6(*c*)). These maximum strain levels for the copper electrode, together with the strain measurement distributions summarized in Fig. 5, present guidelines for PI mesh design, which should meet two requirements: (a) it should be smaller than the elastic stretchability of the Cu electrode

networks, and (b) it should be larger than the maximum skin strain in most regions of the chest. With these criteria, we set the PI mesh to have $R = 500 \,\mu m$, $w_{PI} = 50 \mu m$, $t_{PI} = 100 \,\mu m$, and $\alpha = 110 \deg$. The stress–strain curve of the PI/silbione system is plotted in Fig. 6(*e*) and shows that the transition strain is ~17%, which is smaller than the elastic stretchability of the Cu network but larger than the maximum strain of the skin in most regions.

We conduct two application tests with our strain-limiting substrate-based electrode. First, we adhere the electrode to the chest (Fig. 6(f)) to measure the electrocardiograms of the subject, when the body is fully relaxed (Fig. 6(g)) and those when the four extreme body movements from Figs. 5(a)–5(e) are reached (Figs. 6(h)–6(k)). We clearly observe that the electrode works very well, even when the body undergoes extreme motion. In the second test, the electrode is adhered inside the forearm of the subject (Fig. 6(l)) to measure EMG during hand clenches (Fig. 6(m)). The EMG features are well captured. It is evident that, with our strain-limiting substrate, the stretchable electrode can survive in various skin deformations without mechanical failure, and it is effective in electrophysiological monitoring applications.

3 Conclusions

Effective shielding from excessive mechanical deformations is a requirement for robust stretchable electronic systems. We demonstrate a simple and easy-to-implement strategy for achieving this goal using a nonbuckling-based prestrain-free design for strain-limiting substrates. With our systematic investigation of many geometric factors that determine the mechanical behavior of our strain-limiting substrate, we identify suitable strain-limiting substrates that can be used for skin-mountable stretchable Cu electrodes. This study is expected to offer general guidelines for failure-resistant stretchable electronic platforms.

Appendix A: Experiments

Preparation of Laser-Cut PI Mesh and Cu Electrode Network

Unlike the previous studies where the photolithographic patterning and etching toward the network structures were used [18], the laser cutting process was applied to form all the network layouts used in the present study, including the small-scale PI mesh structures ($15T \times 15T$, $R = 500\,\mu m$, $w_{PI} = 50\,\mu m$, $t_{PI} = 100\,\mu m$, and $\alpha = 180\,deg$) for the tension tests, and large-scale PI ($75T \times 18T$, $R = 500\,\mu m$, $w_{PI} = 50\,\mu m$, $t_{PI} = 100\,\mu m$, and $\alpha = 110\,deg$) and Cu network structures ($L = 1.5R = 1350\,\mu m$, $R = 900\,\mu m$, $w_{Cu} = 50\,\mu m$, $t_{Cu} = 30\,\mu m$, and $\alpha = 180\,deg$) for the stretchable Cu electrode. For the small-scale PI mesh, the laser parameters include the wavelength 525 nm, pulse width 1 ps, and output power 5.5 W. In the cutting process, fifteen scans were conducted, with 1200 mm/s scanning speed and 1200 kHz frequency of the laser scanner, which yields a PI mesh in 56 s. For the large-scale PI mesh, the laser wavelength is 355 nm, pulse width 20 ns, and output power 6.1 W. Twenty scans were conducted, with 600 mm/s scanning speed and 130 kHz frequency of the laser scanner, which yields a PI mesh in 7 min and 23 s. For the Cu network, the laser wavelength is 525 nm, pulse width 1 ps,

and output power 10.3 W. Thirty-five scans were conducted, with 1200 mm/s scanning speed and 1300 kHz frequency of the laser scanner, which yields a Cu network in 2 min and 12 s.

Preparation of Strain-Limiting Substrate and Stretchable Cu Electrode

The PVP (K30) was fully dissolved in the absolute ethyl alcohol to reach saturation. The solution was then coated on a piece of paper, which yields a transparent PVP thin film after volatilization of the ethyl alcohol. A 500 μm thick silbione layer, obtained by 1:1 mixture of two components A and B (silbione RT 4717 A&B, Bluestar silicones, France), was coated on the top of PVP thin film. After the silbione's curing, the paper/PVP/silbione system was immersed in water to dissolve the PVP layer, leading to separation of the silbione layer and the paper. Using a tweezer to transfer the small-scale PI mesh onto the silbione surface, followed by cutting the silbione/PI composite into the desirable shape, defined the strain-limiting substrate, whose tension tests were accomplished by a microtensile material-testing machine (Instron 5848 Microtester) at room temperature. For the stretchable Cu electrode, a silbione thin film was first fabricated as in preparation of strain-limiting substrate. The large-scale PI mesh and two laser-cut Cu electrode networks (with the distance 47 mm) were attached to the top and bottom surfaces, respectively, to finish the fabrication.

Appendix B: Analytic and Numerical Modeling

Analytic Modeling

In a study by Widlund et al. [25], the stretchability of the serpentine structures was analyzed. The developed curved beam model is accurate but complicated. Here, we establish a simple but very practical model to investigate the mechanical behavior and to yield the design criteria for effective strain-limiting substrates.

As shown in Fig. 2(d), according to the Castigliano's theorem, for the PI

$$u = \frac{\partial U_e}{\partial F_{PI}} \tag{B1}$$

where U_e is the strain energy, F_{PI} is the load applied to PI, and u is the displacement associated with F_{PI}. For a quadrant of the PI, we have

$$U_e = \int_0^{\frac{1}{2}\alpha} \frac{M^2(\theta)}{2\overline{EI}_{PI}} R d\theta \tag{B2}$$

where $M(\theta) = F_{PI} R \cos\theta$, $\overline{EI}_{PI} = E_{PI} t_{PI} w_{PI}^3 / 12$, θ is the angular coordinate. Substituting Eq. (B2) into Eq. (B1)

$$u = \int_0^{\frac{1}{2}\alpha} \frac{M(\theta)}{\overline{EI}_{PI}} \frac{\partial M(\theta)}{\partial F_{PI}} R d\theta = \frac{F_{PI} R^3}{4\overline{EI}_{PI}} (\alpha + \sin\alpha) \tag{B3}$$

Since $\varepsilon = u/(R \sin\alpha/2)$, from Eq. (B3), we have

$$F_{PI} = \frac{E_{PI} t_{PI} w_{PI}^3 \sin\frac{\alpha}{2}}{3R^2(\alpha + \sin\alpha)} \varepsilon \tag{B4}$$

For the substrate under uniaxial tension

$$F_{sub} = \overline{EA}_{sub} \frac{u}{R \sin\frac{\alpha}{2}} = \overline{EA}_{sub} \varepsilon \tag{B5}$$

where $\overline{EA}_{sub} = E_{sub} t_{sub} T$, with the cross-sectional area $A_{sub} = t_{sub} T$. Here, the linear stress–strain relationship of the substrate is used for simplification. Although there are, more or less,

some numerical errors, it does not impact the concept of design and the mechanism of the nonbuckling-based strain-limiting substrate. The stress σ in the cross section is

$$\sigma = \frac{F_{PI} + F_{sub}}{A_{sub}} \tag{B6}$$

Substituting Eqs. (B4) and (B5) into Eq. (B6), the stress–strain relationship is obtained as the top line of Eq. (2). After the transition point, the relationships between force increment and strain increment are written as

$$dF_{PI} = \overline{EA}_{PI} \frac{du}{R \sin \frac{\alpha}{2}} = \overline{EA}_{PI} d\varepsilon \tag{B7}$$

and

$$dF_{sub} = \overline{EA}_{sub} d\varepsilon \tag{B8}$$

where $\overline{EA}_{PI} = E_{PI} t_{PI} w_{PI}$ for the PI and substrate, respectively. Therefore, the stress increment $d\sigma$ is

$$d\sigma = \frac{dF_{PI} + dF_{sub}}{A_{sub}} \tag{B9}$$

Substituting Eqs. (B7) and (B8) into Eq. (B9)

$$d\sigma = \frac{\overline{EA}_{PI} + \overline{EA}_{sub}}{A_{sub}} d\varepsilon \tag{B10}$$

Integration of Eq. (B10) gives the bottom line of Eq. (2).

Finite Element Analysis Numerical Modeling

ABAQUS FEA software package [26] was used to study the mechanical behavior of the strain-limiting substrate as well as the stretchable Cu electrode. The compliant elastomeric substrates (ecoflex, PDMS and silbione) were treated as hyper elastic materials depicted by the Mooney–Rivlin model. The stiff films (PI and Cu) were treated as linear elastic and ideal elastic plastic materials, respectively, where the Young's modulus, Poisson's ratio, and yield stress of Cu are $124\,GPa$, 0.34, and $372\,MPa$, respectively. The hexahedron elements C3D8R/C3D6 were adopted for the substrates, and the thin shell element S4R was adopted for PI and Cu. The periodic boundary condition was applied in the modeling shown in Figs. 3 and 6. The meshes of the left and bottom faces of the periodic cell model (i.e., the hexahedron) were copied to their opposite faces, yielding the identical meshes. Each boundary node of the cell was then tied to its associated node of the imaginary neighboring cell by use of the *EQUATION approach in ABAQUS.

References

[1] Kim, D.-H., Ahn, J.-H., Choi, W. M., Kim, H.-S., Kim, T.-H., Song, J., Huang, Y. Y., Liu, Z., Lu, C., and Rogers, J. A., 2008, "Stretchable and Foldable Silicon Integrated Circuits," Science, 320(5875), pp. 507–511.

[2] Li, R., Li, M., Su, Y., Song, J., and Ni, X., 2013, "An Analytical Mechanics Model for the Island-Bridge Structure of Stretchable Electronics," Soft Matter, 9(35), pp. 8476–8482.

[3] Ko, H. C., Stoykovich, M. P., Song, J., Malyarchuk, V., Choi, W. M., Yu, C.-J., Geddes, J. B., III, Xiao, J., Wang, S., Huang, Y., and Rogers, J. A., 2008, "A Hemispherical Electronic Eye Camera Based on Compressible Silicon Optoelectronics," Nature, 454(7205), pp. 748–753.

[4] Song, Y. M., Xie, Y., Malyarchuk, V., Xiao, J., Jung, I., Choi, K.-J., Liu, Z., Park, H., Lu, C., Kim, R.-H., Li, R., Crozier, K. B., Huang, Y., and Rogers, J.

[5] Kim, D.-H., Lu, N., Ma, R., Kim, Y.-S., Kim, R.-H., Wang, S., Wu, J., Won, S. M., Tao, H., Islam, A., Yu, K. J., Kim, T.-I., Chowdhury, R., Ying, M., Xu, L., Li, M., Chung, H.-J., Keum, H., McCormick, M., Liu, P., Zhang, Y.-W., Omenetto, F. G., Huang, Y., Coleman, T., and Rogers, J. A., 2011, "Epidermal Electronics," Science, 333(6044), pp. 838–843.

[6] Ying, M., Bonifas, A. P., Lu, N., Su, Y., Li, R., Cheng, H., Ameen, A., Huang, Y., and Rogers, J. A., 2012, "Silicon Nanomembranes for Fingertip Electronics," Nanotechnol., 23(34), p. 344004.

[7] Su, Y., Li, R., Cheng, H., Ying, M., Bonifas, A. P., Hwang, K.-C., Rogers, J. A., and Huang, Y., 2013, "Mechanics of Finger-Tip Electronics," J. Appl. Phys., 114(16), p. 164511.

[8] Hwang, S.-W., Tao, H., Kim, D.-H., Cheng, H., Song, J.-K., Rill, E., Brenckle, M. A., Panilaitis, B., Won, S. M., Kim, Y.-S., Song, Y. M., Yu, K. J., Ameen, A., Li, R., Su, Y., Yang, M., Kaplan, D. L., Zakin, M. R., Slepian, M. J., Huang, Y., Omenetto, F. G., and Rogers, J. A., 2012, "A Physically Transient Form of Silicon Electronics," Science, 337(6102), pp. 1640–1644.

[9] Li, R., Cheng, H., Su, Y., Hwang, S.-W., Yin, L., Tao, H., Brenckle, M. A., Kim, D.-H., Omenetto, F. G., Rogers, J. A., and Huang, Y., 2013, "An Analytical Model of Reactive Diffusion for Transient Electronics," Adv. Funct. Mater., 23(24), pp. 3106–3114.

[10] Xu, S., Zhang, Y., Cho, J., Lee, J., Huang, X., Jia, L., Fan, J. A., Su, Y., Su, J., Zhang, H., Cheng, H., Lu, B., Yu, C., Chuang, C., Kim, T.-I., Song, T., Shigeta, K., Kang, S., Dagdeviren, C., Petrov, I., Braun, P. V., Huang, Y., Paik, U., and Rogers, J. A., 2013, "Stretchable Batteries With Self-Similar Serpentine Interconnects and Integrated Wireless Recharging Systems," Nat. Commun., 4, p. 1543.

[11] Dagdeviren, C., Yang, B. D., Su, Y., Tran, P. L., Joe, P., Anderson, E., Xia, J., Doraiswamy, V., Dehdashti, B., Feng, X., Lu, B., Poston, R., Khalpey, Z., Ghaffari, R., Huang, Y., Slepian, M. J., and Rogers, J. A., 2014, "Conformal Piezoelectric Energy Harvesting and Storage From Motions of the Heart, Lung, and Diaphragm," Proc. Natl. Acad. Sci. U. S. A., 111(5), pp. 1927–1932.

[12] Su, Y., Dagdeviren, C., and Li, R., 2015, "Measured Output Voltages of Piezoelectric Devices Depend on the Resistance of Voltmeter," Adv. Funct. Mater., 25(33), pp. 5320–5325.

[13] Lu, N., and Kim, D.-H., 2014, "Flexible and Stretchable Electronics Paving the Way for Soft Robotics," Soft Rob., 1(1), pp. 53–62.

[14] Rus, D., and Tolley, M. T., 2015, "Design, Fabrication and Control of Soft Robots," Nature, 521(7553), pp. 467–475.

[15] Gerratt, A. P., Michaud, H. O., and Lacour, S. P., 2015, "Elastomeric Electronic Skin for Prosthetic Tactile Sensation," Adv. Funct. Mater., 25(15), pp. 2287–2295.

[16] Chortos, A., Liu, J., and Bao, Z., 2016, "Pursuing Prosthetic Electronic Skin," Nat. Mater., 15(9), pp. 937–950.

[17] Lee, J., Wu, J., Ryu, J. H., Liu, Z., Meitl, M., Zhang, Y.-W., Huang, Y., and Rogers, J. A., 2012, "Stretchable Semiconductor Technologies With High Areal Coverages and Strain-Limiting Behavior: Demonstration in High-Efficiency Dual-Junction GaInP/GaAs Photovoltaics," Small, 8(12), pp. 1851–1856.

[18] Jang, K.-I., Chung, H. U., Xu, S., Lee, C. H., Luan, H., Jeong, J., Cheng, H., Kim, G.-T., Han, S. Y., Lee, J. W., Kim, J., Cho, M., Miao, F., Yang, Y., Jung, H. N., Flavin, M., Liu, H., Kong, G. W., Yu, K. J., Rhee, S. I., Chung, J., Kim, B., Kwak, J. W., Yun, M. H., Kim, J. Y., Song, Y. M., Paik, U., Zhang, Y., Huang, Y., and Rogers, J. A., 2015, "Soft Network Composite Materials With Deterministic and Bio-Inspired Designs," Nat. Commun., 6, p. 6566.

[19] Gerbode, S. J., Puzey, J. R., McCormick, A. G., and Mahadevan, L., 2012, "How the Cucumber Tendril Coils and Overwinds," Science, 337(6098), pp. 1087–1091.

[20] Chen, P., Xu, Y., He, S., Sun, X., Pan, S., Deng, J., Chen, D., and Peng, H., 2015, "Hierarchically Arranged Helical Fibre Actuators Driven by Solvents and Vapours," Nat. Nanotechnol., 10(12), pp. 1077–1083.

[21] Stoppa, M., and Chiolerio, A., 2014, "Wearable Electronics and Smart Textiles: A Critical Review," Sensors, 14(7), pp. 11957–11992.

[22] Maziz, A., Concas, A., Khaldi, A., Stalhand, J., Persson, N.-K., and Jager, E. W. H., 2017, "Knitting and Weaving Artificial Muscles," Sci. Adv., 3(1), p. e1600327.

[23] Ma, Y., Jang, K.-I., Wang, L., Jung, H. N., Kwak, J. W., Xue, Y., Chen, H., Yang, Y., Shi, D., Feng, X., Rogers, J. A., and Huang, Y., 2016, "Design of Strain-Limiting Substrate Materials for Stretchable and Flexible Electronics," Adv. Funct. Mater., 26(29), pp. 5345–5351.

[24] Su, Y., Ping, X., Yu, K. J., Lee, J. W., Fan, J. A., Wang, B., Li, M., Li, R., Harburg, D. V., Huang, Y., Yu, C., Mao, S., Shim, J., Yang, Q., Lee, P.-Y., Armonas, A., Choi, K.-J., Yang, Y., Paik, U., Chang, T., Dawidczyk, T. J., Huang, Y., Wang, S., and Rogers, J. A., 2017, "In-Plane Deformation Mechanics for Highly Stretchable Electronics," Adv. Mater., 29(8), p. 1604989.

[25] Widlund, T., Yang, S. X., Hsu, Y. Y., and Lu, N. S., 2014, "Stretchability and Compliance of Freestanding Serpentine-Shaped Ribbons," Int. J. Solids Struct., 51(23–24), pp. 4026–4037.

[26] ABAQUS, 2013, "Analysis User's Guide V6.13," Dassault Systèmes, Vélizy-Villacoublay, France.